Full Length Article

Bridge sulfur vacancies in MoS$_2$ catalyst for reverse water gas shift: A first-principles study

Hai-Yan Su [a], Keju Sun [b,*], Jin-Xun Liu [c], Xiufang Ma [d], Minzhen Jian [c], Chenghua Sun [e], Yongjun Xu [a], Huibin Yin [a], Wei-Xue Li [c,*]

[a] School of Chemical Engineering and Energy Technology, Dongguan University of Technology, Dongguan 523808, China
[b] Key Laboratory of Applied Chemistry, School of Environmental and Chemical Engineering, Yanshan University, 438 Hebei Avenue, Qinhuangdao 066004, China
[c] Department of Chemical Physics, School of Chemistry and Materials Science, Hefei National Laboratory for Physical Sciences at the Microscale, iChEM, CAS Center for Excellence in Nanoscience, University of Science and Technology of China, Hefei 230026, China
[d] Shenzhen Key Laboratory of Advanced Thin Films and Applications, College of Physics and Optoelectronic Engineering, Shenzhen University, Shenzhen 518060, China
[e] Centre for Translational Atomaterials, Swinburne University of Technology, Hawthorn, Victoria 3122, Australia

A B S T R A C T

Vacancies, typically exist in various types and morphologies on the surfaces of transition metal compound catalysts, have been shown to play an important role in many catalytic reactions. However, identifying the optimal type and morphology of vacancy and the key factors that control its performance remains a significant challenge. By density functional theory calculations and microkinetic modeling, we show that compared to various threefold S vacancy morphologies on the basal plane, the lower coordination number at the bridge S vacancy of Mo edge on MoS$_2$ tunes the relative adsorption strength of key intermediates (such as O relative to OH). This not only increases CO$_2$ hydrogenation rate by 7–11 orders of magnitude, but also leads to clearly distinct mechanism (associative & redox). The large destabilization of O and low H coverage on the Mo edge also hinder C-O scission and hydrogenation (give CH$_4$ and CH$_3$OH) relative to CO desorption, leading to almost 100% CO selectivity. The inexpensive MoS$_2$ catalyst provides an alternative to the traditional noble metal catalysts for reverse water gas shift, and the coordination number of vacancy modulated catalytic performance illustrates a promising way to design transition metal compound catalysts for other important reactions of technological interest.

1. Introduction

Vacancy, as one common type of surface defects, has been suggested to play an important role in many catalytic reactions on the transition metal compound catalysts [1–11]. A variety of types and morphologies of vacancies often coexist on the surfaces of these catalysts, and the identification of the optimal vacancy remains a significant challenge because of difficulties in controllably creating vacancies with specific structure experimentally. The combination of DFT calculations and microkinetic modeling to establish a direct link between the reaction rate and the type and morphology of vacancy, can not only identify the optimal vacancy structure but also provide mechanistic insight into the key factor that govern the catalytic activity at the atomic level. The fundamental understanding will greatly accelerate the design and development of transition metal compound catalysts.

A single layer of MoS$_2$ (denoted by MoS$_2$ hereafter), which typically contains distinct types and morphologies of sulfur vacancies, is chosen to illustrate the relation between the vacancy structure and catalytic performance. The sulfur vacancies on MoS$_2$ can generally be divided into two types: threefold sulfur vacancy on the basal plane and bridge sulfur vacancy on the edges (Mo edge or S edge) [10–15], in which the Mo atoms have different coordination number with the adsorbates (CN = 3 vs 2, see Fig. 1). In addition, for a given type of sulfur vacancy, such as the threefold sulfur vacancy on the basal plane, various morphologies have been observed by scanning tunneling microscopy/spectroscopy after high-temperature annealing at about 900 K [13]. Several representative morphologies of threefold sulfur vacancies on the MoS$_2$ basal plane, including two, three, four and six neighboring sulfur vacancies, are shown in Fig. 1a, c, e-i. Despite the same coordination number with adsorbates (CN = 3), the favorable threefold sulfur vacancies in these

morphologies differ in the number of S atoms coordinated to Mo atoms (N_S, see below for a sample calculation). The variation in CN and N_S, caused by the distinct types and morphologies of sulfur vacancies on the MoS_2 catalyst, may have a significant impact on the adsorption of intermediates and catalytic activity.

A few studies have shown that MoS_2 catalysts are active in CO_2 hydrogenation [16–18], by which CO_2 is transformed into energy-rich commodities, not only addresses the "3Rs" (reduce, reuse, and recycle) associated with the increasing CO_2 emissions, but also provides a promising way for the sustainable development of long-term fossil-carbon industries [19–21]. In particular, CO_2 hydrogenation to CO and H_2O, namely the reverse water gas shift (RWGS) reaction, has recently attracted much attention as its importance in converting CO_2 to chemicals or liquid fuels through the industrially developed methanol and Fischer−Tropsch synthesis [22,23]. Despite the studies, the optimal type and morphology of sulfur vacancy on MoS_2 and the key factor controlling its activity and selectivity in RWGS remains unclear. In addition, the inexpensive MoS_2 catalyst also provides an alternative to the reducible oxide supported noble metal catalysts that are commonly used in RWGS, which leave ample room for improvement, particularly in terms of price [24–28].

By density functional theory (DFT) calculations and microkinetic modeling, we show that regardless of the morphologies of the threefold sulfur vacancies on the MoS_2 basal plane the relatively strong O binding causes O poisoning and low CO_2 hydrogenation rate at 580–780 K, 1 bar and H_2/CO_2 ratio of 1. With decreasing CN at the bridge sulfur vacancy of the Mo edge, the O is greatly destabilized, leading to facile O removal and moderate CO_2 dissociation activity via both associative and redox route, thereby increasing the total CO_2 hydrogenation rate by 7–11 orders of magnitude compared with the MoS_2 basal plane. At the same time, the weakened O adsorption and low H coverage on the Mo edge also suppress C-O scission and hydrogenation for CH_4 and CH_3OH formation, leading to almost 100% CO selectivity. The work opens up a new avenue for non-precious metal catalyst development in RWGS, and the insights obtained can be applied to design and develop transition metal compound catalysts for other important reactions of technological interest.

2. Methods

Spin-polarized DFT calculations were performed with the VASP [29] with PBE [30]. The interaction between the ionic cores and electrons was described by the projector-augmented wave (PAW) method [31], and the Kohn-Sham valence electronic wavefunction was expanded in a plane-wave basis set with a kinetic energy cutoff at 400 eV. The lattice constants for bulk 2H-MoS_2 were calculated to be a = b = 3.19 Å, c = 12.43 Å, in agreement with the experimental values (a = b = 3.16 Å, c = 12.29 Å) [32].

The morphologies of the threefold S vacancies on the (0 0 1) basal plane of the S−Mo−S trilayer were modeled using the (5 × 3) unit cells with two, three, four and six adjacent S vacancies (denoted by $MoS_2(001)\_2v$, $MoS_2(001)\_3v$, $MoS_2(001)\_3v_1$, $MoS_2(001)\_3v_2$, $MoS_2(001)\_4v$ and $MoS_2(001)\_6v$), as shown in Fig. 1a, c, e-i. The eight-layer (4 × 1) MoS_2(1 0 0) surfaces with 38% and 50% S coverage were used to model the bridge S vacancies on the Mo edge (Fig. 1b and d) and S edge. Systematic investigations showed a large reconfiguration at the transition states (TSs) of elementary reactions in CO_2 hydrogenation, particularly for the C-O bond scission reactions on the S edge. Thus, we only employ the Mo edge below to illustrate the bridge S vacancy type. The surface Brillouin zone was sampled with a (2 × 3 × 1) and (2 × 2 × 1) Monkhorst-Pack k-points grid mesh for MoS_2(0 0 1) and MoS_2(1 0 0) surface, respectively [33]. Neighboring slabs were separated by a vacuum of 15 Å to avoid the interactions between them. All the atoms in adsorbates and slabs were relaxed till the residual forces were < 0.03 eV/Å. The adsorption energy (ΔE_{Ads}) was calculated using the most stable adsorption configurations (E_{total}) relative to the clean surfaces (E_{slab}) and the isolated adsorbates (E_{ad}) unless otherwise indicated:

$$\Delta E_{Ads} = E_{total} - E_{slab} - E_{ad} \tag{1}$$

A lower (more negative) ΔE_{Ads} implies stronger binding, while a higher (more positive) ΔE_{Ads} implies weaker binding.

All transition states (TSs) were located by the climbing-image nudged elastic band method (CI-NEB) [34] and force reversed method [35]. The relaxation will stop until the residual forces in each atom were smaller than 0.03 eV/Å. The elementary activation barrier (ΔE_{Act}) and reaction energy (ΔH) were calculated with respect to the separate adsorption state of adsorbates on the surfaces.

Microkinetic simulations are performed by the MKMCXX program [36]. Zero-point energy (ZPE) corrections are included in the microkinetic simulations. We mostly focus on RWGS, and the typical RWGS reaction conditions of 580–780 K, 1 bar and $H_2/CO_2 = 1$ are employed in the microkinetic simulations. A detailed description of the microkinetic simulation is shown in Supporting Information.
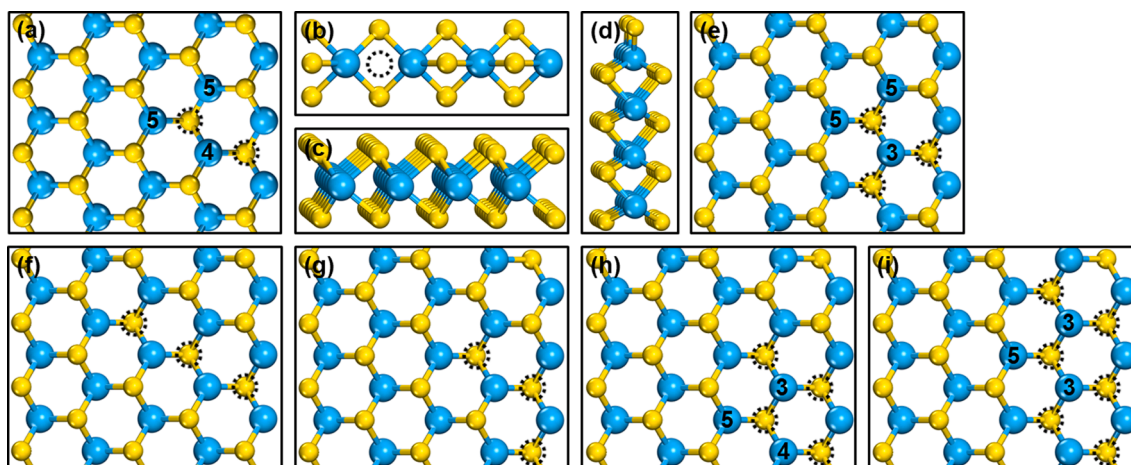

Fig. 1. Top view of (a) $MoS_2(001)\_2v$ and (b) Mo edge, side view of (c) $MoS_2(001)\_2v$ and (d) Mo edge, and top view of (e) $MoS_2(001)\_3v$, (f) $MoS_2(001)\_3v_1$, (g) $MoS_2(001)\_3v_2$, (h) $MoS_2(001)\_4v$ and (i) $MoS_2(001)\_6v$. The blue and yellow balls and black circles represent Mo and S atoms and S vacancies, respectively. The number of S atoms coordinated to Mo atoms at the S vacancies are denoted.

3. Results and discussion

3.1. Structures of sulfur vacancies on single layer MoS₂ Surface.

A single layer MoS_2 consists of an S-Mo-S sandwich, where the Mo atoms are arranged in a hexagonal lattice with a trigonal prismatic coordination with respect to the two S layers. The perfect MoS_2 basal plane, with each Mo atom coordinated to six S atoms, is always catalytically inert. Many studies have been devoted to create the threefold sulfur vacancies through low-energy argon sputtering, electron irradiation or pretreatment at high-temperature or reductive atmosphere in order to enhance the catalytic activity of MoS_2 basal plane [12–15]. For instance, the scanning tunneling microscopy/spectroscopy study show that the vacancy chains, with number of S vacancies ranging from 2 to 4, can be generated on monolayer MoS_2 as-grown on Au foils by thermal annealing at high temperature ($\approx$ 900 K) [13]. Furthermore, the structures of the sulfur vacancies have also been shown to be stable after CO_2 hydrogenation at 453 K, 50 bar and a H_2/CO_2 ratio of 3 by high-angle annular dark field scanning transmission electron microscopy measurements [14]. Based on the experimental findings, we simulate several representative arrangement of threefold S vacancies, including two, three, four or six adjacent S vacancies on the MoS_2 basal plane, denoted by $MoS_2(001)\_2v$, $MoS_2(001)\_3v$, $MoS_2(001)\_3v_1$, $MoS_2(001)\_3v_2$, $MoS_2(001)\_4v$ and $MoS_2(001)\_6v$, respectively, as shown in Fig. 1a, c, e-i (see Method Section for more details). We also calculate the formation free energies of vacancies ($\triangle G_{Vac}$) for various structures studied at 573 K in the presence of H_2/H_2S (1 bar/10^{-8} bar). As listed in Table S1, the average $\triangle G_{Vac}$ on $MoS_2(001)\_2v$ is calculated to be 0.99 eV. With increasing vacancy concentration, the average $\triangle G_{Vac}$ gradually increases, with the maximum of 1.23 eV on $MoS_2(001)\_6v$. These results indicate that the formation of S vacancy on the basal plane is quite difficult, which can rationalize well with the rigorous experimental conditions for its creation [12–15]. Moreover, as the concentration of vacancy increases, its formation becomes more difficult. Although the favorable threefold sulfur vacancies on the $MoS_2(001)$ surfaces have the same coordination number with adsorbates (CN = 3), they differ in the number of S atoms coordinated to Mo atoms (N_S), as we will show below.

Besides the threefold S vacancies (CN = 3) on the basal plane, the bridge S vacancies (CN = 2) can expose on the low-Miller index edges of MoS_2, which have been identified as the active sites for many catalytic reactions, such as hydrodesulfurization and CO hydrogenation [10,11,37]. The Mo-edge site with 42%-50% S coverage has been used to simulate hydrodesulfurization and CO hydrogenation under the reductive atmosphere. Since CO hydrogenation has similar reaction conditions and intermediates as CO_2 hydrogenation reaction, the selection of its model can be used as a reference for the present system. In a previous work, a (7 × 1) $MoS_2(100)$ surface with a 42% S coverage has been used to simulate the Mo edge for CO hydrogenation [37]. To reduce the cost of computation, a (4 × 1) $MoS_2(100)$ surface with 38% S coverage is employed to model the bridge S vacancy on the Mo edge in the present work (Fig. 1b and d). The differential $\triangle G_{Vac}$ on this surface is calculated to be −0.46 eV, suggesting that the formation of S vacancy on the Mo edge is more facile than on the basal plane. In the next sections, we will first address the effect of S vacancy types, namely the threefold S vacancy on the MoS_2 basal surface and the bridge S vacancy on the Mo edge (characterized by CN) on CO_2 hydrogenation, and then reveal the effect of the morphologies of threefold S vacancies on the MoS_2 basal surface (characterized by N_S).

3.2. Effect of sulfur vacancy types on RWGS.

In this section, the threefold S vacancy on $MoS_2(001)\_2v$ and the bridge S vacancy on the Mo edge are chosen to illustrate the effect of S vacancy types. We mainly focus on RWGS, and the other CO_2 hydrogenation reactions including methane and methanol synthesis are also

addressed to complete the picture. We first study the adsorption of various intermediates involved in CO_2 hydrogenation on $MoS_2(001)\_2v$ and Mo edge, and the adsorption energies ΔE_{Ads} and favorable adsorption structures are shown in Table S2, Fig. 2 and our previous work [38]. The intermediates can be divided into two groups: (1) In Group I, the adsorption of the intermediates, such as CH_xO ($x = 1$–3), OH, CO_x ($x = 1$, 2), HCOO and CH_3, do not exhibit a strong dependence on the type of S vacancy, as shown in Fig. 3a. Note that a higher bar in Fig. 3 corresponds a weaker adsorption, whereas a lower bar corresponds a stronger adsorption. The variation in the ΔE_{Ads} of the intermediates (see ΔE in Fig. 3a) between $MoS_2(001)\_2v$ and Mo edge falls in the region of −0.02–0.39 eV. This can be well understood because many adsorbates in this group bind to the surfaces by single-bond (CH_3O, OH and CH_3), where the variation in CN of S vacancies has only a slight effect on their ΔE_{Ads}. (2) The intermediates (Group II), such as O, CH, COH, CH_2 and CHOH, have more unpaired electrons to bind with the surfaces, and their adsorption are highly sensitive to the CN of S vacancies. As shown in Fig. 3b, these intermediates bind significantly weaker with decreasing CN of S vacancies from $MoS_2(001)\_2v$ (CN = 3) to Mo edge (CN = 2). O and CH show the largest increase in ΔE_{Ads}, by 1.73 and 1.02 eV, respectively. The Bader charge analysis show that the Mo atoms transfer more electrons to O (0.89e) at the threefold S vacancy on $MoS_2(001)\_2v$ than at the bridge S vacancy on Mo edge (0.82e). These results correspond well to the projected density of states (PDOS) analysis in Fig. 4a, where no states are available at the Fermi level of the Mo atoms upon O adsorption on $MoS_2(001)\_2v$, in contrast with Mo edge. The variation of ΔE_{Ads} as CN of S vacancies reflects the double or triple bond nature induced by more unpaired electrons in the adsorbates, leading to their preference to bond with more surface Mo atoms. In addition, the ΔE_{Ads} of H_2O, COOH and CH_2OH decreases as the CN of S vacancies decrease. For instance, H_2O has a ΔE_{Ads} of −0.84 eV at the S vacancy of the Mo edge, substantially lower than that on $MoS_2(001)\_2v$ by 0.73 eV. These results can be rationalized well with the more significant electron donation from the lone pair electrons of O ($2p_z$) in H_2O to the empty $4d$-states at the Mo atom on the Mo edge than on $MoS_2(001)\_2v$, as seen from the deep-lying orbital hybridization at the energy window: [−8 eV to −6 eV] in Fig. 4b. This may be due to the fact that the Mo atom at the Mo edge coordinates with fewer S atoms, leading to more empty $4d$-states available to accept the lone pair electrons of O in H_2O.

The ΔE_{Ads} of intermediates are closely related to the reaction energies ΔH of the involving elementary reaction steps. For an elementary reaction $A^*+^* \rightarrow B^*+C^*$, the ΔH is given by Eq. (2):

$$\Delta H = E_{B^*} + E_{C^*} - E_{A^*} - E_*$$
$$= (E_{B^*} - E_B - E_*) + (E_{C^*} - E_C - E_*) - (E_{A^*} - E_A - E_*) + (E_B + E_C - E_A)$$
$$= \Delta E_{Ads}(B) + \Delta E_{Ads}(C) - \Delta E_{Ads}(A) + R$$

(2)

where E_{B^*}, E_{C^*}, E_{A^*} and E_* are the total energy of adsorbed B, C and A and clean surface, and E_B, E_C and E_A are the total energy of B, C and A in gas phase. $R = E_B + E_C - E_A$ is independent of the surfaces. Thus, the variation of ΔH between different surfaces is determined by the variation of ΔE_{Ads} (ΔE) of intermediates.

By calculating the ΔE of the various intermediates between $MoS_2(001)\_2v$ and Mo edge (see Fig. 3), we find that the ΔH of C-O scission in CO_2, CH_xO ($x = 1$, 2) and HCOO, and OH_x ($x = 0$, 1) hydrogenation, which are crucial in determining the activity and selectivity for CO_2 hydrogenation, can be significantly tuned by the CN of S vacancies on the MoS_2 catalyst. The C-O scission reactions have very large ΔE for the products such as O and CH_x ($x = 1$, 2), as shown in Fig. 3b, while maintain a relatively small ΔE for the reactants (Fig. 3a) as the CN of S vacancies decrease from $MoS_2(001)\_2v$ (CN = 3) to Mo edge (CN = 2). As a result, these reactions on the Mo edge become more endothermic than on $MoS_2(001)\_2v$ by 1.81–3.03 eV (Fig. 5a). The less favorable thermodynamics on the Mo edge also results in more difficult C-O scission kinetics. For instance, the activation energies ΔE_{Act} of CHO
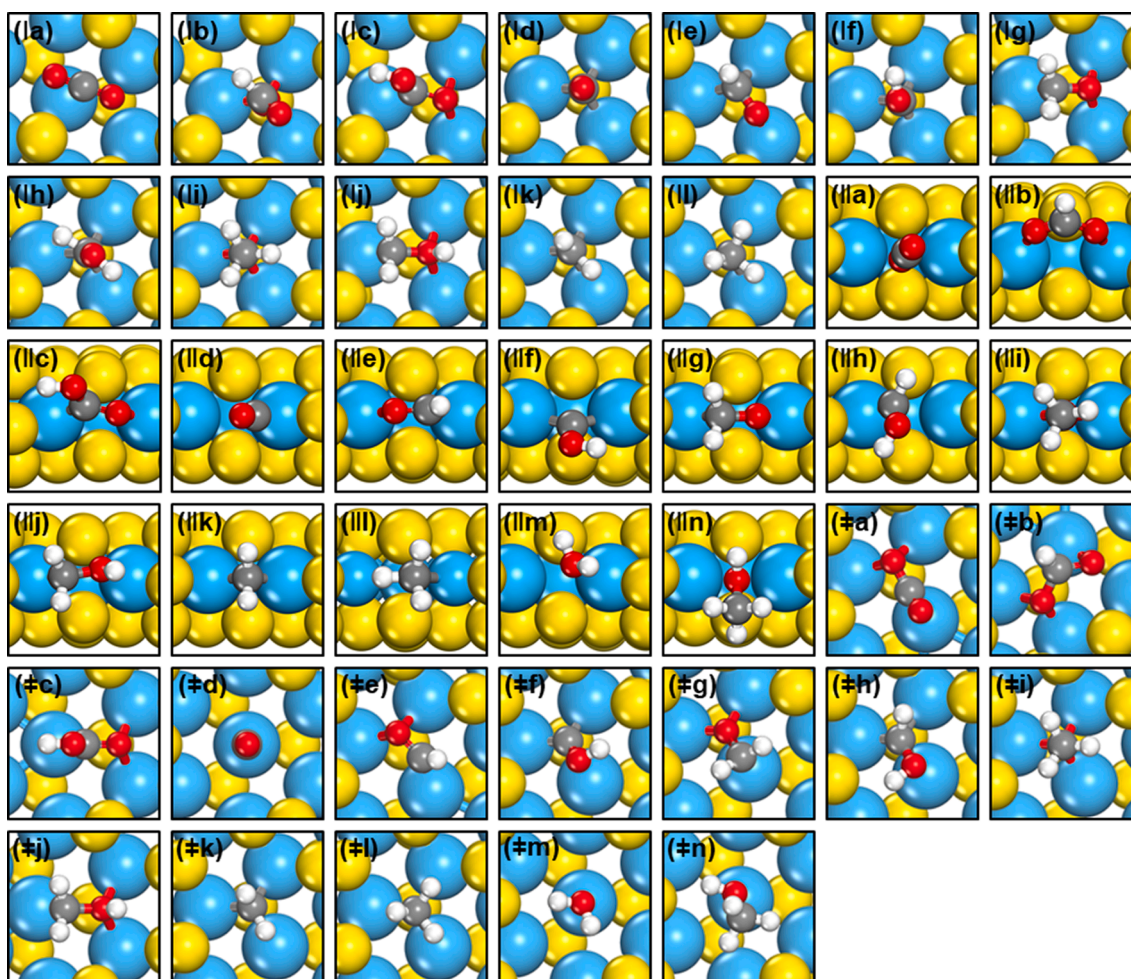
Fig. 2. Optimized configurations for (a) CO_2 (b) HCOO (c) COOH (d) CO (e) CHO (f) COH (g) CH_2O (h) CHOH (i) CH_3O (j) CH_2OH (k) CH_2 (l) CH_3 (m) H_2O (n) CH_3OH adsorption on $MoS_2(001)\_2v$ (I), Mo edge (II) and $MoS_2(001)\_3v$ (‡). The blue, yellow, grey, red and white balls represent Mo, S, C, O and H atoms, respectively.
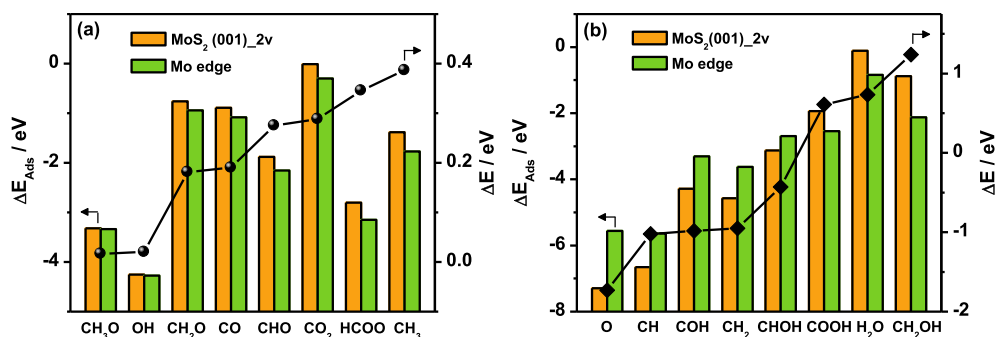

Fig. 3. The adsorption energies ΔE_{Ads} of species (bar) and their difference ΔE (line + symbol) between $MoS_2(001)\_2v$ and Mo edge in (a) Group I and (b) Group II. Black circle and cube represent ΔE in Group I and Group II, respectively.

and CO_2 dissociation on the Mo edge are 1.08 and 0.94 eV (see Fig. 5b), much higher than the corresponding values (0.40 and 0.47 eV) on $MoS_2(001)\_2v$. On the other hand, when the adsorption of reactant rather than product is sensitive to CN of S vacancies (large ΔE as CN), such as O hydrogenation reaction, the ΔH and ΔE_{Act} show the reverse trend with CN as the C-O scission reactions. As shown in Fig. 5c and 5d, not only is O hydrogenation more exothermic on the Mo edge compared with $MoS_2(001)\_2v$, but the ΔE_{Act} is also lower on the Mo edge (0.36 vs 1.78 eV). In addition, for the OH hydrogenation reaction, with OH binding slightly depended on CN, the stronger binding of H_2O on the Mo

edge results in smaller ΔH and ΔE_{Act} (by 1.07 and 0.92 eV) than on $MoS_2(001)\_2v$, as shown in Fig. 5c and 5d. According to the analysis, the elementary pathways in the redox mechanism, such as OH_x ($x = 0, 1$) hydrogenation and CO_2 decomposition to CO, have modest ΔE_{Act} on the Mo edge, and thus an improved RWGS activity compared to $MoS_2(001)\_2v$ can be expected.

To achieve a complete catalytic cycle for CO_2 hydrogenation reaction, we also investigate other elementary reactions on $MoS_2(001)\_2v$ and Mo edge. The energetics and structures at the TSs are shown in Table 1 and 2 and Figure S1, S2, 6a and 6b. Two possible mechanisms,
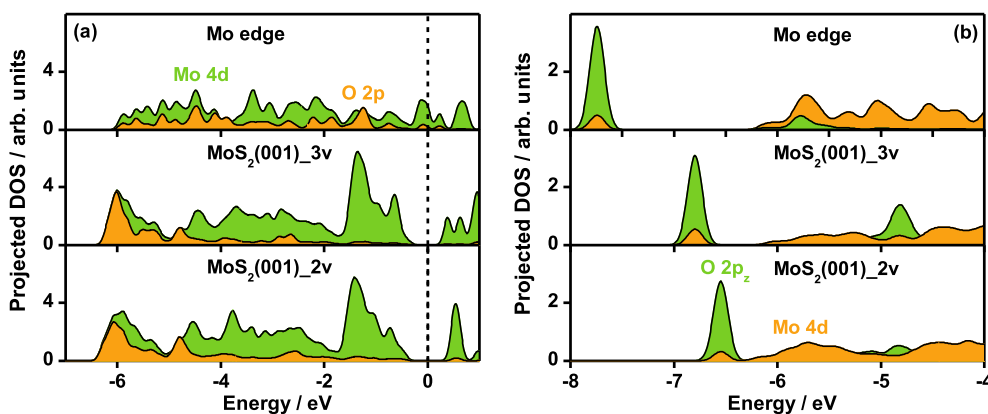
Fig. 4. Projected density of states of (a) O and (b) H_2O adsorption at the S vacancies on $MoS_2(001)\_2v$, $MoS_2(001)\_3v$ and Mo edge. The total $2p$ and $2p_z$ states of O are shown for O and H_2O adsorption, respectively. The total $4d$ states of Mo that bind to adsorbates at the corresponding S vacancies are shown.
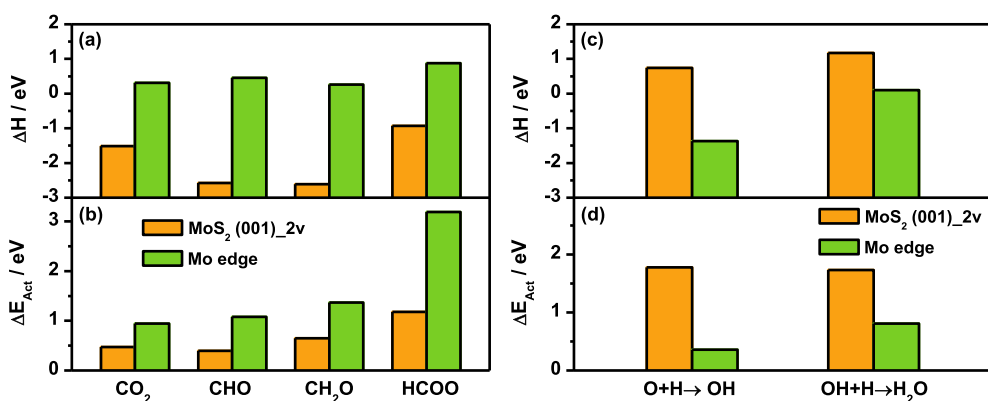

Fig. 5. The reaction energies ΔH and activation energies ΔE_{Act} for C-O scission in CO_2, CHO, CH_2O and HCOO (a, b) and OH_x ($x = 0, 1$) hydrogenation (c, d) on $MoS_2(001)\_2v$ and Mo edge.

namely redox mechanism and associative mechanism, for RWGS have been proposed [39,40], and they differ with each other in CO_2 activation by direct or hydrogen-assisted pathway via the intermediates such as formate (HCOO) or carboxyl (COOH). The redox mechanism involves the direct CO_2 decomposition into CO and O, with the ΔE_{Act} of 0.47 and 0.94 eV on $MoS_2(001)\_2v$ and Mo edge, as shown above. The atomic O can be removed through H_2O either by two successive H addition steps or by one H addition followed by disproportionation of two OH species. The above discussions have shown that O removal by the former pathway is quite facile on the Mo edge, while has very high ΔE_{Act} on $MoS_2(001)\_2v$. In contrast, OH disproportionation has a lower ΔE_{Act} than its hydrogenation by 0.47 eV on $MoS_2(001)\_2v$, suggesting that the latter pathway is preferred on this surface.

According to the associative mechanism, atomic H addition to CO_2 leads to the formation of HCOO or COOH intermediate, which then undergoes the C-O bond scission to produce CHO or COH/CO. Subsequently, the H abstraction from CHO or COH leads to CO formation. Both the formation and decomposition of HCOO/COOH have fairly high barriers (1.03–1.47 eV) on $MoS_2(001)\_2v$, indicating that the associative mechanism is less favorable than the redox mechanism. On the Mo edge, although HCOO and COOH formation are quite facile (0.92 and 0.44 eV), the high ΔE_{Act} (3.19 and 2.75 eV) for their decomposition to CHO and COH hinder the H-assisted CO_2 activation pathways. However, COOH decomposition to CO has a small ΔE_{Act} of 0.65 eV, which dominates the associative mechanism. The minimum energy pathways for RWGS on $MoS_2(001)\_2v$ and Mo edge are shown in Fig. 6a, 6b and Scheme 1. Remarkably, the redox mechanism is predominant on $MoS_2(001)\_2v$, whereas both redox and associative ($CO_2 + H \rightarrow COOH \rightarrow CO$) mechanism may contribute to RWGS on the Mo edge.

We now turn to the methane and methanol formation pathways. According to the above discussions, adsorbed CO is a key intermediate for RWGS on $MoS_2(001)\_2v$ and Mo edge. The adsorbed CO can either desorb or react further, leading to the formation of methane and methanol. The possible pathways we considered for methane or methanol formation are listed in Table 1 and 2, and the minimum energy pathways on $MoS_2(001)\_2v$ and Mo edge are shown in Fig. 6a, 6b and Scheme 1. The methane formation proceeds via same pathways on the two surfaces. Namely, H addition to CO leads to the formation of CHO, which then goes through C-O scission followed by three successive H addition steps. The methanol formation pathways on the two surfaces are slightly different. CHO prefers a hydrogen addition at the O end, followed by two successive H addition at the C end on $MoS_2(001)\_2v$, whereas the reverse is found on the Mo edge. It can be seen from Table 1 and 2 that the hydrogenation reactions generally have lower ΔE_{Act} on Mo edge than on $MoS_2(001)\_2v$. This can be well understood because the H adsorbs at the S site on the Mo edge, which has a 0.34 eV higher ΔE_{Ads} than on $MoS_2(001)\_2v$ with H adsorption at the S vacancy.

Based on the DFT calculated energetics, a microkinetic simulation is conducted at typical RWGS conditions (580–780 K, 1 bar, $H_2/CO_2 = 1$). A detailed description of the microkinetic model is given in Supporting Information. Regardless of temperatures, the direct CO_2 dissociation is at least 3 orders of magnitude faster than the H-assist CO_2 dissociation via HCOO or COOH on $MoS_2(001)\_2v$ (see Table 1), which is due to the low CO_2 dissociation barrier (0.47 eV). Once CO is produced, it prefers to desorb instead of react further to yield methane or methanol. The former is substantially faster than the latter two pathways, leading to almost 100% CO selectivity at the temperatures considered, as shown in Figure S3a. On the Mo edge, the CO_2 dissociation pathways are

Table 1
Activation Energies (ΔE_{Act}, in eV) and Reaction Energies (ΔH, in eV) of Various Elementary Reactions in CO_2 Hydrogenation on $MoS_2(001)\_2v$ and $MoS_2(001)\_3v$. * and X* Denote the Vacant S Vacancy and Adsorbed X Species at the S Vacancy, Respectively. The Calculated Rates (r, in $s^{-1}site^{-1}$) of the Elementary Steps in the Microkinetic Study at 720 K, 1 bar and H_2/CO_2 Ratio of 1 Are Listed. The gaseous and adsorbed H_2O/CH_3OH are used for $MoS_2(001)\_2v$ and $MoS_2(001)\_3v$, respectively.

Elementary reactions	$MoS_2(001)\_2v$				$MoS_2(001)\_3v$			
	ΔE_{Act}	ΔH	r	DRC	ΔE_{Act}	ΔH	r	DRC
$CO_2*+*=CO*+O*$	0.47	−1.52	6.54×10^{-11}	−1.36	0.27	−2.28	1.10×10^{-9}	−0.84
$O*+H*=OH*+*$	1.78	0.74	1.31×10^{-10}		1.96	0.86	2.21×10^{-9}	0.69
$OH*+H*=H_2O + 2*/H_2O*+*$	1.73	1.28	1.00×10^{-13}		1.69	0.68	1.87×10^{-14}	1.17
$2OH*=H_2O + O*+*/H_2O*+O*$	1.26	0.53	6.54×10^{-11}	1.36	1.03	−0.18	1.10×10^{-9}	
$CO_2+*=HCOO*+*$	1.47	−0.17	$<10^{-14}$	1.00				
$CO_2*+H*=COOH*+*$	1.35	0.31	$<10^{-14}$					
$HCOO*+*=CHO*+O*$	1.18	−0.93	$<10^{-14}$					
$COOH*+*=CO*+OH*$	1.14	−1.08	$<10^{-14}$					
$COOH*+*=COH*+O*$	1.03	−1.97	$<10^{-14}$					
$CHO*+*=CH*+O*$	0.40	−2.58	$<10^{-14}$	0.17	0.56	−2.52	$<10^{-14}$	0.40
$CH_2O*+*=CH_2*+O*$	0.65	−2.61	$<10^{-14}$		0.70	−1.97	$<10^{-14}$	
$CHOH*+*=CH*+OH*$	0.97	−1.55	$<10^{-14}$		0.43	−1.55	$<10^{-14}$	0.27
$CH_3O*+*=CH_3*+O*$	0.98	−0.61	$<10^{-14}$		0.97	−1.08	$<10^{-14}$	
$CH_2OH*+*=CH_2*+OH*$	0.63	−2.73	$<10^{-14}$		0.49	−2.34	$<10^{-14}$	
$CH*+H*=CH_2*+*$	0.22	−0.25	$<10^{-14}$		0.37	−0.21	$<10^{-14}$	
$CH_2*+H*=CH_3*+*$	1.05	0.82	$<10^{-14}$		1.08	0.64	$<10^{-14}$	
$CH_3*+H*=CH_4 + 2*$	0.83	−0.74	$<10^{-14}$	0.72	0.59	−0.16	$<10^{-14}$	
$CO*+H*=CHO*+*$	0.81	0.42	$<10^{-14}$	−0.88	1.54	1.05	$<10^{-14}$	0.13
$CO*+H*=COH*+*$	1.03	−0.15	$<10^{-14}$		1.43	0.62	$<10^{-14}$	
$CHO*+H*=CH_2O*+*$	0.79	−0.22	$<10^{-14}$		0.50	−0.76	$<10^{-14}$	0.08
$CHO*+H*=CHOH*+*$	1.07	−0.28	$<10^{-14}$		0.58	−0.10	$<10^{-14}$	
$COH*+H*=CHOH*+*$	0.48	0.29	$<10^{-14}$		0.80	0.33	$<10^{-14}$	0.10
$CH_2O*+H*=CH_3O*+*$	0.66	−1.19	$<10^{-14}$		0.65	−0.24	$<10^{-14}$	
$CH_2O*+H*=CH_2OH*+*$	1.54	0.87	$<10^{-14}$					
$CHOH*+H*=CH_2OH*+*$	1.34	0.93	$<10^{-14}$		1.35	0.57	$<10^{-14}$	
$CH_3O*+H*=CH_3OH + 2*/CH_3OH*+*$	1.72	1.26	$<10^{-14}$		1.73	0.78	$<10^{-14}$	
$CH_2OH*+H*=CH_3OH + 2*/CH_3OH*+*$	0.74	−0.79	$<10^{-14}$		0.90	−0.70	$<10^{-14}$	
$CO*=CO+*$							1.10×10^{-9}	−1.00

Table 2
Activation Energies (ΔE_{Act}, in eV) and Reaction Energies (ΔH, in eV) of Various Elementary Reactions in CO_2 Hydrogenation on the Mo Edge. *, #, X* and H# Denote the Vacant S Vacancy and S Site, Adsorbed X Species at the S Vacancy and Adsorbed H at the S Site, Respectively. The Calculated Rates of the Elementary Steps in the Microkinetic Study at 720 K (r, in $s^{-1}site^{-1}$), 1 bar and H_2/CO_2 Ratio of 1 Are Listed.

Reactions	ΔE_{Act}	ΔH	r	DRC
$CO_2*+*=CO*+O*$	0.94	0.31	1.99×10^{-2}	0.79
$H_2*+\#=H*+H\#$	0.43	0.07	2.50×10^{-2}	
$H*+\#=*+H\#$	0.66	0.34	2.50×10^{-2}	
$O*+H\#=OH*+\#$	0.36	−1.37	2.04×10^{-2}	
$OH*+H\#=H_2O*+\#$	0.81	0.10	2.50×10^{-2}	
$CO_2*+H\#=HCOO*+\#$	0.92	−0.59	$<10^{-14}$	
$CO_2*+H\#=COOH*+\#$	0.44	−0.37	5.08×10^{-3}	0.13
$HCOO*+*=CHO*+O*$	3.19	0.88	$<10^{-14}$	
$COOH*+*=CO*+OH*$	0.65	−0.68	5.08×10^{-3}	0.07
$COOH*+*=COH*+O*$	2.75	1.35	$<10^{-14}$	
$CHO*+*=CH*+O*$	1.08	0.45	6.74×10^{-13}	0.99
$CH_2O*+*=CH_2*+O*$	1.37	0.26	$<10^{-14}$	
$CHOH*+*=CH*+OH*$	0.56	−0.98	$<10^{-14}$	
$CH_2OH*+*=CH_2*+OH*$	0.79	−0.56	$<10^{-14}$	
$CH*+H\#=CH_2*+\#$	0.73	−0.68	6.77×10^{-13}	
$CH_2*+H\#=CH_3*+\#$	0.36	−0.88	6.79×10^{-13}	
$CH_3*+H\#=CH_4+*+\#$	0.61	−0.72	6.79×10^{-13}	
$CO*+H\#=CHO*+\#$	0.50	−0.02	6.79×10^{-13}	
$CO*+H\#=COH*+\#$	1.24	0.67	$<10^{-14}$	
$CHO*+H\#=CH_2O*+\#$	0.83	−0.49	$<10^{-14}$	
$CHO*+H\#=CHOH*+\#$	0.82	0.06	$<10^{-14}$	
$CH_2O*+H\#=CH_2OH*+\#$	0.37	−0.55	$<10^{-14}$	
$CHOH*+H\#=CH_2OH*+\#$	0.41	−1.10	$<10^{-14}$	
$CH_2O*+H\#=CH_3O*+\#$	0.75	−1.38	$<10^{-14}$	
$CH_3O*+H\#=CH_3OH*+\#$	0.90	−0.04	$<10^{-14}$	
$CH_2OH*+H\#=CH_3OH*+\#$	0.88	−0.87	$<10^{-14}$	
$CO*=CO+*$			2.50×10^{-2}	−1.00

temperature dependent. The H-assisted CO_2 dissociation pathway via COOH is faster than the direct CO_2 dissociation pathway by 1.2–2.5 times at temperatures below 620 K. At higher temperatures, the direct CO_2 dissociation pathway is more favorable (Table 2). Correspondingly, both associative and redox mechanism contribute to RWGS on the Mo edge. In both mechanisms, CO is a key intermediate via which methane and methanol are produced. Similarly to $MoS_2(001)\_2v$, the CO on the Mo edge prefers to desorb instead of react further to yield methane and methanol. The rate of CO formation is 10 orders of magnitude higher than that of CH_4 formation, which is much faster than CH_3OH formation at the temperatures studied, leading to almost complete CO_2 conversion to CO on the Mo edge, as shown in Figure S3b. According to the microkinetic modeling, the CO_2 hydrogenation rate on the Mo edge is 7–11 orders of magnitude faster than that on $MoS_2(001)\_2v$ (see Fig. 7a, Table 1 and 2), and CO is the predominant product on both $MoS_2(001)$ _2v and Mo edge regardless of temperatures. The simulated selectivity is in excellent with the experimental findings on MoS_2 catalysts, where the selectivity to CO is more than 99.5% in the total flow rate of 10–80 ml. min^{-1} at 773 K and H_2/CO_2 ratio of 1 [16].

The steady-state surface coverages on $MoS_2(001)\_2v$ and Mo edge are given in Fig. 8. Regardless of temperatures the $MoS_2(001)\_2v$ surface is dominantly covered with O (Fig. 8a) owing to the strong O adsorption. The O poisoning also results in the low activity of RWGS on this surface. The Mo edge is mainly covered with the vacant S sites (#) and S vacancies (*) and H*, as shown in Fig. 8b. As the temperatures increase, the concentration of the vacant S vacancies (*) gradually increase at the expense of H* concentration. This can be well understood since the high temperatures facilitated the diffusion of H* to H#. It is interesting to compare the coverage of * and H#, which largely determine the selectivity of methane and methanol on the Mo edge. As shown in Fig. 6b, the CHO intermediate, produced by CO hydrogenation, either decomposes into CH (leads to CH_4) or hydrogenates to CH_2O (leads to CH_3OH) as following:
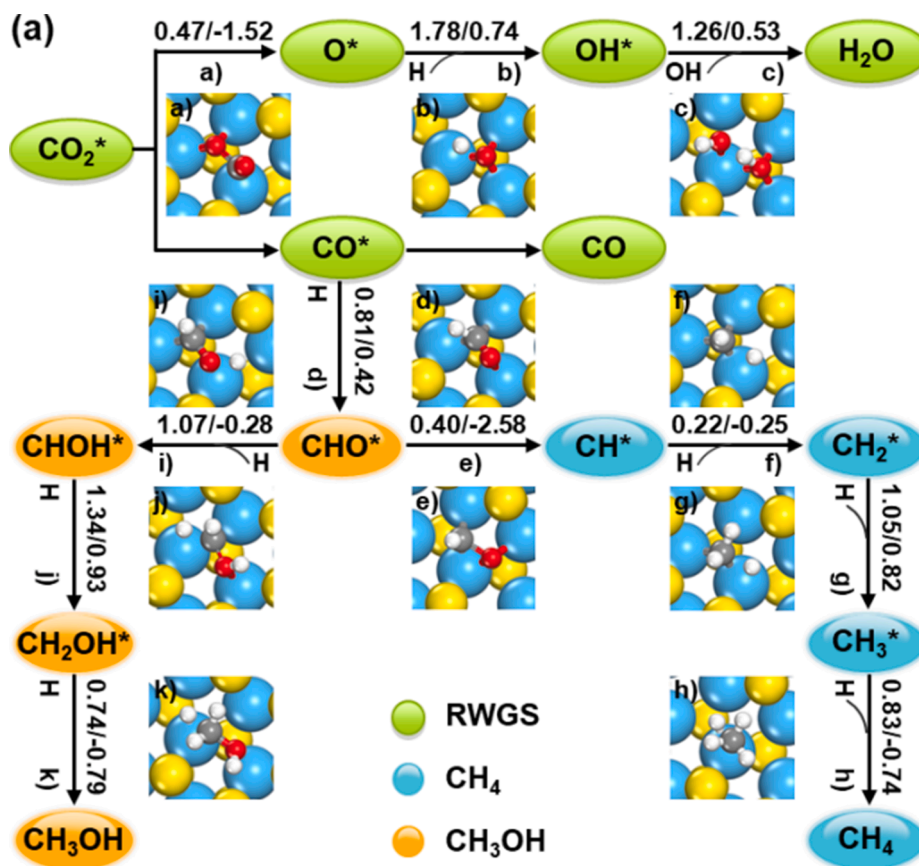
Fig. 6. Schematic of the optimal reaction pathways for CO_2 hydrogenation on (a) $MoS_2(001)\_2v$, (b) Mo edge and (c) $MoS_2(001)\_3v$. A/B represents activation energy/reaction energy in the unit of eV. The transition state structure of each elementary reaction is also shown.

$$CHO^* + * \rightarrow CH^* + O^* \tag{3}$$

$$CHO^* + H^\# \rightarrow CH_2O^* + \# \tag{4}$$

We estimate the selectivity (S) of CH_4 and CH_3OH by the ratio of C-O scission rate r_1 and the hydrogenation rate r_2 of CHO:

$$S = \frac{r_1}{r_2} = \frac{k_1\theta_*}{k_2\theta_{H^\#}} = \frac{A_1}{A_2}e^{\frac{(\Delta E_{Act2} - \Delta E_{Act1})}{RT}}\frac{\theta_*}{\theta_{H^\#}} \tag{5}$$

where ΔE_{Act} is the activation energy, A is the pre-exponential factor, which is assumed to be the same on both the sites, and θ is the coverage. Although the CHO hydrogenation barrier is lower than its C-O scission barrier by 0.25 eV, the substantially higher concentration of * compared with $H^\#$ (by 4 orders of magnitude) results in more favorable CH_4 formation than CH_3OH formation on the Mo edge.

The degree of rate control (DRC) of step (*i*) $X_{RC,i}$, which can qualitatively determine the significance of single step (*i*) in the overall reaction, is defined as

$$X_{RC,i} = \frac{k_i}{r}\left(\frac{\partial r}{\partial k_i}\right)_{k_{j\neq i}, K_i} = \left(\frac{\partial lnr}{\partial lnk_i}\right)_{k_{j\neq i}, K_i} \tag{6}$$

where k_i, K_i and r are the forward rate constant, the equilibrium constant for elementary step i and the reaction rate, respectively [41]. A positive value of DRC for a particular step means that this step is a rate limiting step, and the decrease in the ΔE_{Act} would increase the overall rate. A negative value indicates the opposite, and such steps are termed inhibition steps. Lowering the barriers of such steps decreases the overall

rate. The steps with absolute DRC values larger than 0.01 are shown. Fig. 7b shows that regardless of temperatures the CO_2 consumption rate on $MoS_2(001)\_2v$ is mostly determined by H_2O removal through OH disproportionation. This can be assigned to the high ΔE_{Act} for OH formation ($\Delta E_{Act} = 1.78$ eV), leading to its low coverage on $MoS_2(001)\_2v$. In addition, HCOO formation, C-O scission in CHO and CH_3 hydrogenation are also important to control CO_2 consumption rate. It can be seen that these steps are related to the H-assisted CO_2 dissociation mechanism. The decrease in the ΔE_{Act} of these steps can suppress the direct CO_2 dissociation mechanism and the causing O poisoning problem. Rate-inhibiting reactions also occur. For instance, the direct CO_2 dissociation inhibits the reaction rate, because lowering the barrier of this step leads to more severe O poisoning. On the Mo edge, the C-O scission in CHO mainly determines the reaction rate at the temperatures considered (Fig. 7c), owing to its high ΔE_{Act} of 1.08 eV. In addition, direct CO_2 dissociation, COOH formation and decomposition are also important to control the reaction rate, which correspond to two CO_2 activation mechanisms (redox vs associative) on the surface. At temperatures below 620 K, COOH formation has a larger DRC value than direct CO_2 dissociation, whereas the opposite order is found at higher temperatures. This rationalizes well with the dominant associative and redox mechanism at the temperatures below and above 620 K. On the other hand, the DRC analysis also indicates that the increased CO coverage will suppress the CO_2 consumption rate. The C-O scission as rate-controlling steps on the Mo edge agree well with previous steady-state kinetics studies on MoS_2 catalysts [17].

Based on DFT calculations and microkinetic modeling, we show that the enhanced RWGS activity is achieved by modulating the CN of S

(b)

CO$_2$* → [0.44/-0.37, H, a)] → COOH* → [0.65/-0.68, c)] → OH* → [0.81/0.10, H, d)] → H$_2$O*

CO$_2$* → [0.94/0.31, b)] → CO* → CO

COOH* → [c)] → CO*

CO* → [0.50/-0.02, H, e)] → CHO*

CHO* → [0.83/-0.49, j), H] → CH$_2$O*

CHO* → [1.08/0.45, f)] → CH*

CH* → [0.73/-0.68, H, g)] → CH$_2$*

CH$_2$O* → [0.75/-1.38, H, k)] → CH$_3$O*

CH$_3$O* → [0.90/-0.04, H, l)] → CH$_3$OH*

CH$_2$* → [0.36/-0.88, H, h)] → CH$_3$*

CH$_3$* → [0.61/-0.72, H, i)] → CH$_4$

Legend:
- RWGS (green)
- CH$_4$ (blue)
- CH$_3$OH (orange)

(c)

CO$_2$* → [0.27/-2.28, a)] → O* → [1.96/0.86, H, b)] → OH* → [1.03/-0.18, OH, c)] → H$_2$O*

CO$_2$* → CO*

CO* → CO

CO* → [1.43/0.62, H, d)] → COH*

CO* → [1.54/1.05, H, j)] → CHO*

COH* → [0.80/0.33, H, e)] → CHOH*

CHO* → [0.50/-0.76, k), H] → CH$_2$O*

CHOH* → [0.43/-1.55, f)] → CH*

CH$_2$O* → [0.65/-0.24, H, l)] → CH$_3$O*

CH$_3$O* → [1.73/0.78, H, m)] → CH$_3$OH*

CH* → [0.37/-0.21, H, g)] → CH$_2$*

CH$_2$* → [1.08/0.64, h), H] → CH$_3$*

CH$_3$* → [0.59/-0.16, H, i)] → CH$_4$

Legend:
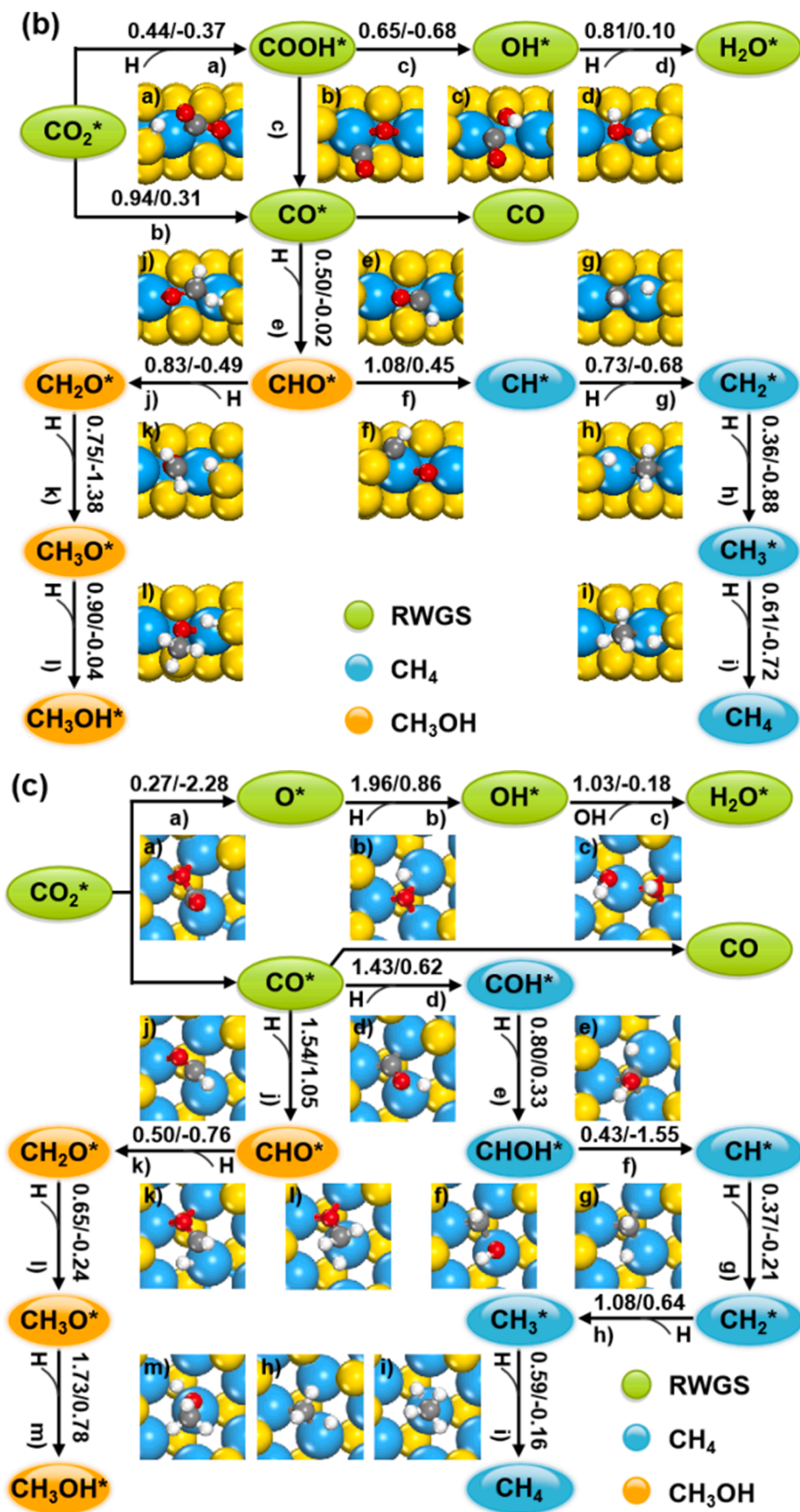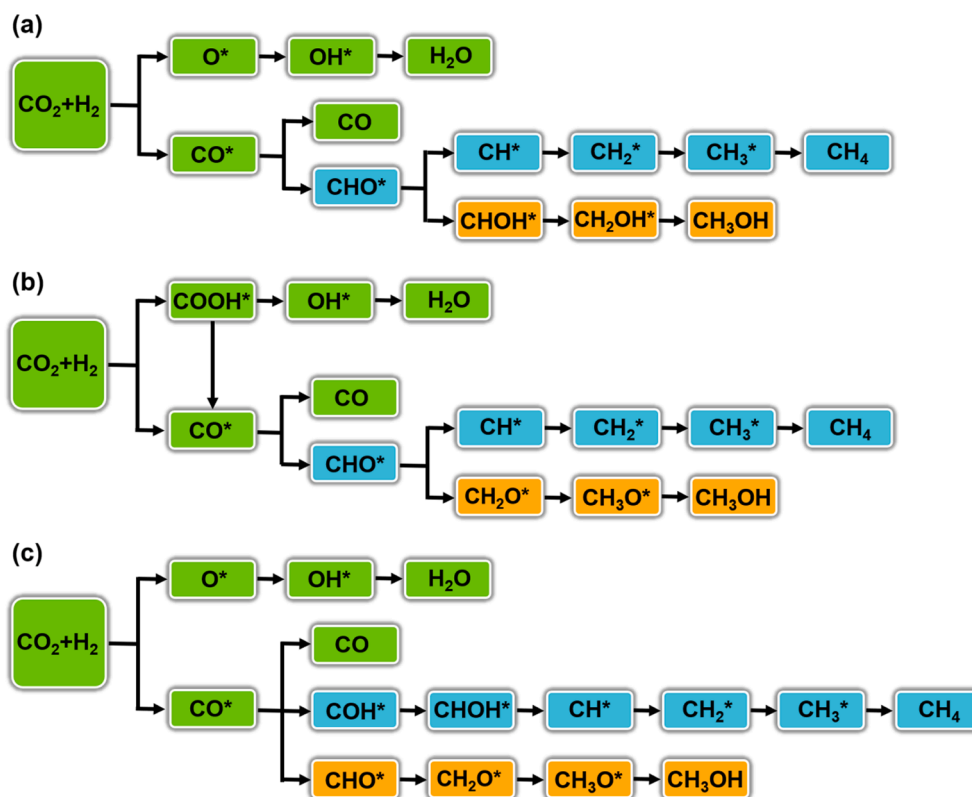- RWGS (green)
- CH$_4$ (blue)
- CH$_3$OH (orange)

Fig. 6. (*continued*).

Scheme 1. The optimal reaction pathways for RWGS (green) and CH₄ (blue) and CH₃OH (yellow) synthesis from CO₂ hydrogenation on (a) MoS₂(001)_2v, (b) Mo edge and (c) MoS₂(001)_3v.
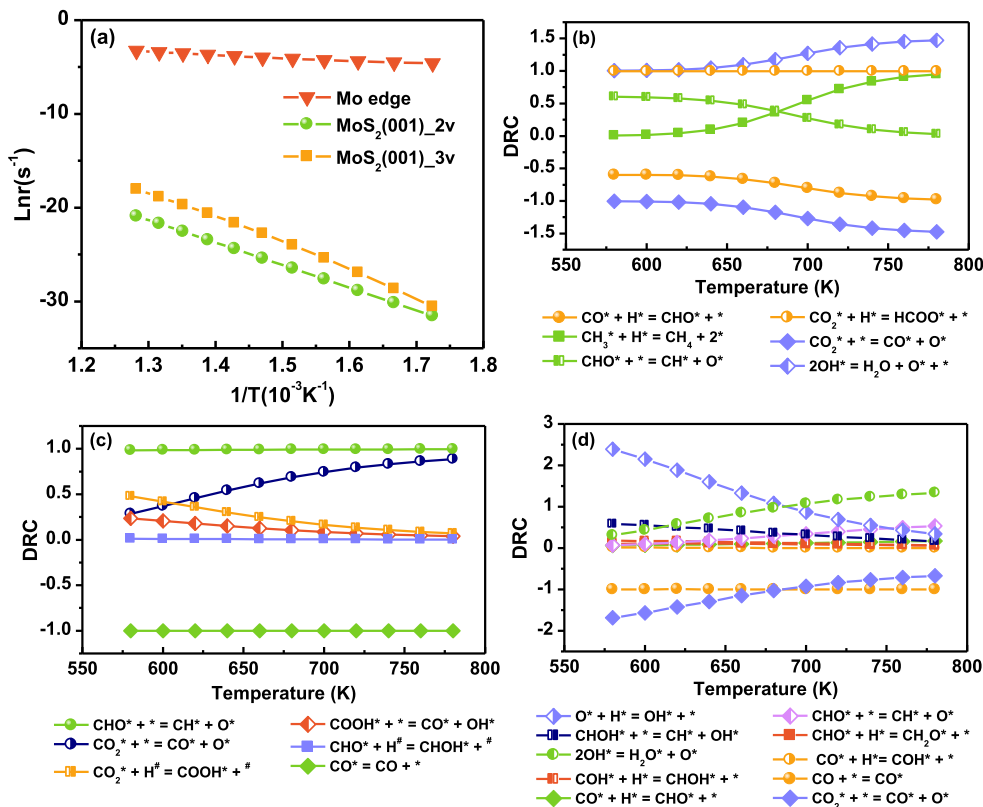

Fig. 7. (a) The reaction rate of CO_2 hydrogenation and the degree of rate control (DRC) of the elementary steps for CO_2 hydrogenation on (b) MoS₂(0 0 1)_2v, (c) Mo edge and (d) MoS₂(0 0 1)_3v as a function of temperature via microkinetic modeling. ZPE corrections are included.
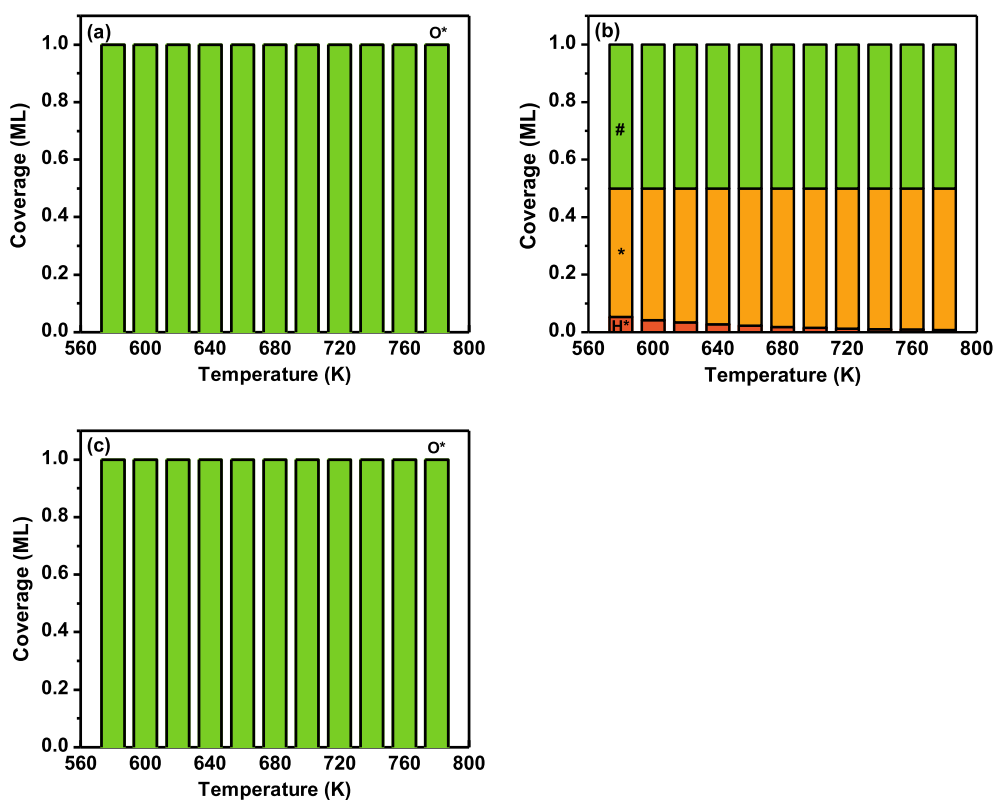
Fig. 8. The coverage of intermediates as a function of temperature on (a) $MoS_2(001)\_2v$, (b) Mo edge and (c) $MoS_2(001)\_3v$. # and * represent the S sites and S vacancies, respectively.

vacancies on the MoS_2 catalyst. This bridge S vacancy (CN = 2) on the Mo edge significantly destabilizes O, leading to a lower O saturation coverage than on $MoS_2(001)\_2v$ with the threefold S vacancy (CN = 3), thereby providing more adsorbate free active sites where reactants can be activated. At the same time, this decrease in CN of S vacancy greatly accelerates the O removal and CO_2 hydrogenation reaction through a substantial destabilization of the adsorbed O. The weakened O adsorption and low H coverage on the Mo edge also suppress the C-O scission and hydrogenation that favor CH_4 and CH_3OH formation, leading to high selectivity of CO.

3.3. Effect of sulfur vacancy morphologies on RWGS.

Having studied the effect of S vacancy types on CO_2 hydrogenation, we now turn our attention to that of S vacancy morphologies. We primarily focus on the different morphologies of the threefold S vacancies on $MoS_2(001)\_2v$, $MoS_2(001)\_3v$, $MoS_2(001)\_3v_1$, $MoS_2(001)\_3v_2$, $MoS_2(001)\_4v$ and $MoS_2(001)\_6v$ (see Fig. 1a, 1c, 1e-i). The number of S atoms coordinated to Mo atoms (N_S) at the favorable threefold S vacancies on the $MoS_2(001)$ surfaces vary from each other, which may affect the intermediates adsorption and elementary reaction steps.

Compared to $MoS_2(001)\_2v$, the variation in the magnitude of ΔE_{Ads} of the intermediates at the favorable sites (Figure S4) on $MoS_2(001)\_3v_1$ and $MoS_2(001)\_3v_2$ is rather small, i.e., not greater than 0.29 eV for all the fifteen adsorbates, as listed in Table 3 and S2. However, on $MoS_2(001)\_3v$, the ΔE_{Ads} of some adsorbates are noticeably different from those on $MoS_2(001)\_2v$. For instance, $MoS_2(001)\_3v$ binds CO, H_2O, CH_xOH ($x = 2, 3$) and CH_2O considerably stronger than $MoS_2(001)\_2v$ by 0.69–1.08 eV (see Fig. 2 for the adsorption configurations). This may be attributed to the less coordination with S atoms at the Mo atom on $MoS_2(001)\_3v$, resulting in the more empty $4d$-states available to accept the electrons from these adsorbates, as seen from the more significant orbitals hybridization (-7 eV to −6 eV) between O $2p_z$

and Mo $4d$ in the PDOS analysis for H_2O adsorption in Fig. 4b.

The energetics and structures at the TSs of the various elementary reaction steps in CO_2 hydrogenation on $MoS_2(001)\_3v_1$, $MoS_2(001)\_3v_2$ and $MoS_2(001)\_3v$ are shown in Table 1 and S3 and Fig. 6c, S5 and S6. Similarly to $MoS_2(001)\_2v$, the direct CO_2 decomposition to CO and O on the three surfaces are very facile, with small ΔE_{Act} of 0.23–0.34 eV; the O and OH removal on the three surfaces are very difficult, and the ΔE_{Act} fall in the range of 1.03–2.04 eV. These results suggest that the redox mechanism will be preferred, and the rate of RWGS will be very low on the three surfaces, which are similar to $MoS_2(001)\_2v$. Besides the CO_2 dissociation and O and OH removal reactions, the other elementary reaction steps on $MoS_2(001)\_3v_1$ and $MoS_2(001)\_3v_2$ have comparable ΔE_{Act} as those on $MoS_2(001)\_2v$, with the greatest variation in ΔE_{Act} by 0.36 eV (see Table 1 and S3). Therefore, it can be speculated that the selectivity on $MoS_2(001)\_3v_1$ and $MoS_2(001)\_3v_2$ are very similar to that on $MoS_2(001)\_2v$, that is, CO would be the dominant product on the two surfaces. However, some elementary steps such as CH_xO ($x = 0, 1$) hydrogenation and CHOH decomposition have large variation in the ΔE_{Act} (by at most 0.73 eV) between $MoS_2(001)\_3v$ and $MoS_2(001)\_2v$, which make us to recall the large variation in the ΔE_{Ads} of some adsorbates between the two surfaces as shown above. Taken together, the $MoS_2(001)\_3v$ surface might deserve a thorough study.

We then systematically investigate the elementary reaction steps involved in CO_2 hydrogenation on $MoS_2(001)\_3v$, and use the DFT results (Table 1, Fig. 6c and Scheme 1) to perform the microkinetic modeling. The calculated rates of the elementary steps in the microkinetic study at 720 K, 1 bar and H_2/CO_2 ratio of 1 are listed in Table 1. It can be seen that the rate of RWGS on $MoS_2(001)\_3v$ is about 3–17 times faster than that on $MoS_2(001)\_2v$, which mainly originate from its lower OH disproportionation barrier (1.03 vs 1.26 eV). The rate of RWGS is at least 5 orders of magnitude higher than that of methane and methanol formation on $MoS_2(001)\_3v$, suggesting that CO formation is favored over CH_4 and CH_3OH formation, as shown in Figure S3c. Compared with

MoS$_2$(001)_2v, the selectivity on MoS$_2$(001)_3v remains unchanged. This may be due to that not only CO desorption (leads to RWGS) but also CO hydrogenation to CHO (leads to CH$_4$ and CH$_3$OH) becomes more difficult on MoS$_2$(001)_3v than on MoS$_2$(001)_2v, as seen from the ΔE_{Ads} of CO (-1.86 vs −0.89 eV) and the ΔE_{Act} of CHO formation (1.54 vs 0.81 eV) on the two surfaces. It can be seen from Fig. 8c that irrespective of temperatures the MoS$_2$(001)_3v surface is predominantly covered with O, which can be attributed to its strong O adsorption. Likewise, the O poisoning also causes the low activity of RWGS on MoS$_2$(001)_3v as on MoS$_2$(001)_2v.

Fig. 7d shows that the CO$_2$ consumption rate on MoS$_2$(001)_3v is mostly determined by O hydrogenation at temperatures below 680 K owing to its high ΔE_{Act} of 1.96 eV. With increasing temperatures (700–780 K), OH disproportionation becomes more important in controlling CO$_2$ consumption rate. In contrast, the direct CO$_2$ dissociation inhibits the reaction rate, because lowering the barrier of this step leads to more severe O poisoning. Additionally, the increased CO coverage will also inhibit the CO$_2$ consumption rate.

Compared to MoS$_2$(001)_3v, the ΔE_{Ads} of the intermediates progressively decrease (with the exception of H$_2$O and CHOH) with increasing vacancy content on MoS$_2$(001)_4v and MoS$_2$(001)_6v (see Table 3 and Figure S7). Since the O removal limits the CO$_2$ hydrogenation rate on MoS$_2$(001)_2v and MoS$_2$(001)_3v, we will only summarize the adsorption of intermediates associated with O removal reactions on MoS$_2$(001)_4v and MoS$_2$(001)_6v below. As listed in Table 3, atomic hydrogen has an ΔE_{Ads} of −0.73 and −0.84 eV with respect to 1/2H$_2$ in gas phase on MoS$_2$(001)_4v and MoS$_2$(001)_6v, much lower than the ΔE_{Ads} on MoS$_2$(001)_3v by 0.30 and 0.41 eV. Compared to atomic hydrogen, the decrease of the ΔE_{Ads} of O and OH with the vacancy content are smaller, by 0.09–0.21 eV and 0.16–0.27 eV, respectively, as seen from the corresponding values on MoS$_2$(001)_4v, MoS$_2$(001)_6v and MoS$_2$(001)_3v in Table 3. Binding of H$_2$O on MoS$_2$(001)_4v (ΔE_{Ads} = -0.87 eV), MoS$_2$(001)_6v (ΔE_{Ads} = -0.85 eV) and MoS$_2$(001)_3v (ΔE_{Ads} = -0.90 eV) is quasidegenerate.

The stronger intermediates binding on MoS$_2$(001)_4v and MoS$_2$(001)_6v also lead to more difficult O removal. As listed in Table 4, not only are O + H reactions more endothermic on MoS$_2$(001)_4v and MoS$_2$(001)_6v compared with MoS$_2$(001)_3v, but the ΔE_{Act} are also increased by 0.08 and 0.29 eV on MoS$_2$(001)_4v and MoS$_2$(001)_6v (see Figure S8 for the TSs structures). Likewise, the ΔE_{Act} of OH hydrogenation and disproportionation on MoS$_2$(001)_4v and MoS$_2$(001)_6v are 0.26–0.63 eV and 0.10–0.19 eV higher than on MoS$_2$(001)_3v. In addition, we note that the direct CO$_2$ decomposition to CO and O has

Table 4
Activation Energies (ΔE_{Act}, in eV) and Reaction Energies (ΔH, in eV) of Various Elementary Reactions in CO$_2$ Hydrogenation on MoS$_2$(001)_4v and MoS$_2$(001)_6v. * and X* Denote the Vacant S Vacancy and Adsorbed X Species at the S Vacancy, Respectively.

Elementary reactions	MoS$_2$(001)_4v			MoS$_2$(001)_6v	
	ΔE_{Act}	ΔH		ΔE_{Act}	ΔH
CO$_2$*+*=CO*+O*	0.28	−2.10		0.34	−2.02
O*+H*=OH*+*	2.04	0.93		2.25	1.22
OH*+H*=H$_2$O*+*	1.95	1.02		2.32	1.42
2OH*=H$_2$O*+O*	1.22	0.09		1.13	0.20
CHO*+*=CH*+O*	0.32	−2.06		0.48	−2.09
CH$_2$O*+*=CH$_2$*+O*	0.70	−2.04		0.79	−2.17
CHOH*+*=CH*+OH*	0.60	−1.96			
CH$_3$O*+*=CH$_3$*+O*	1.04	−1.47		1.12	−1.73
CH$_2$OH*+*=CH$_2$*+OH*	0.88	−2.54			
CH*+H*=CH$_2$*+*	0.55	−0.03		0.90	0.30
CH$_2$*+H*=CH$_3$*+*	0.66	0.40		0.94	0.56
CH$_3$*+H*=CH$_4$ + 2*	1.11	0.47		1.59	1.01
CO*+H*=CHO*+*	1.28	0.63		1.01	0.70
CO*+H*=COH*+*	1.53	0.82			
CHO*+H*=CH$_2$O*+*	0.94	−0.06		0.89	0.38
CHO*+H*=CHOH*+*	1.37	0.83			
COH*+H*=CHOH*+*	0.70	0.63			
CH$_2$O*+H*=CH$_3$O*+*	0.73	−0.17		0.95	0.12
CHOH*+H*=CH$_2$OH*+*	0.93	0.54			
CH$_3$O*+H*=CH$_3$OH*+*	2.04	1.05		2.21	1.45
CH$_2$OH*+H*=CH$_3$OH*+*	0.98	−0.55			

rather small ΔE_{Act} (0.28 vs 0.34 eV) on MoS$_2$(001)_4v and MoS$_2$(001)_6v, which is slightly higher than the value of 0.27 eV on MoS$_2$(001)_3v. These results indicate that the redox mechanism may also be dominant for RWGS on MoS$_2$(001)_4v and MoS$_2$(001)_6v, and the strong O and OH adsorption largely lower the CO$_2$ hydrogenation rate on the two surfaces.

Our calculations have shown that regardless of the morphologies of sulfur vacancies studied on the MoS$_2$(001) surfaces the binding of O (-7.27 ~ -7.73 eV) is so strong that it would poison CO$_2$ hydrogenation reaction. To identify the key factors that control the O adsorption, we employ the number of S atoms coordinated to Mo atoms (N$_S$) at the threefold S vacancies on the MoS$_2$(001) surfaces, as in our previous work for OH/MnO$_x$ systems [42]. We take MoS$_2$(001)_2v as a sample to illustrate how to calculate N$_S$ at the preferred S vacancies for O adsorption. The three surface Mo atoms at the favorable S vacancis bind with five, five and four S atoms (as denoted in Fig. 1a), respectively, and each S atom binds with three Mo atoms. Thereafter, N$_S$ is calculated as:

Table 3
Calculated Adsorption Energies (ΔE_{Ads}, in eV) and Favorable Adsorption Sites of Various Intermediates on MoS$_2$(001)_3v_1, MoS$_2$(001)_3v_2, MoS$_2$(001)_3v, MoS$_2$(001)_4v and MoS$_2$(001)_6v. The ΔE_{Ads} of H Is Calculated with Respect to 1/2H$_2$ in Gas Phase.

| Species	MoS$_2$(001)_3v_1		MoS$_2$(001)_3v_2		MoS$_2$(001)_3v		MoS$_2$(001)_4v		MoS$_2$(001)_6v	
	ΔE_{Ads}	Site	ΔE_{Ads}	Site	ΔE_{Ads}	Site	ΔE_{Ads}	Site	ΔE_{Ads}	Site
H	−0.32	hcp	−0.40	hcp	−0.43	hcp	−0.73	fcc	−0.84	fcc
CO$_2$					−0.44	O$_{bri}$-C$_{top}$	−0.86	C$_{top}$-O$_{bri}$	−1.15	O$_{top}$-O$_{top}$
CO	−0.90	C$_{hcp}$	−1.10	C$_{hcp}$	−1.86	C$_{top}$	−2.00	C$_{top}$	−2.09	C$_{top}$
O	−7.27	hcp	−7.29	hcp	−7.52	hcp	−7.61	hcp	−7.73	hcp
OH	−4.36	O$_{hcp}$	−4.48	O$_{hcp}$	−4.46	O$_{hcp}$	−4.62	O$_{hcp}$	−4.73	O$_{hcp}$
H$_2$O					−0.90	O$_{top}$	−0.87	O$_{top}$	−0.85	O$_{top}$
CHO	−1.89	C$_{bri}$-O$_{top}$	−2.17	C$_{top}$-O$_{bri}$	−2.32	C$_{top}$-O$_{bri}$	−3.03	C$_{bri}$-O$_{bri}$	−3.32	C$_{top}$-O$_{bri}$
COH	−4.30	C$_{hcp}$	−4.31	C$_{hcp}$	−4.59	C$_{hcp}$	−4.66	C$_{hcp}$	−4.68	C$_{hcp}$
CH$_2$O	−0.88	C$_{top}$-O$_{bri}$			−1.84	C$_{top}$-O$_{hcp}$	−1.98	C$_{top}$-O$_{hcp}$	−2.11	C$_{top}$-O$_{hcp}$
CHOH	−3.12	C$_{hcp}$	−3.12	C$_{hcp}$	−3.49	C$_{hcp}$-O$_{top}$	−3.39	C$_{bri}$	−4.02	C$_{hcp}$
CH$_3$O	−3.44	O$_{hcp}$			−3.56	O$_{hcp}$	−3.76	O$_{hcp}$	−3.87	O$_{hcp}$
CH$_2$OH	−0.99	C$_{top}$-O$_{bri}$	−1.14	C$_{top}$-O$_{bri}$	−1.70	C$_{top}$-O$_{bri}$	−1.77	C$_{top}$-O$_{bri}$	−2.26	C$_{bri}$-O$_{top}$
CH$_3$OH					−0.82	O$_{top}$	−0.88	O$_{top}$	−0.87	O$_{top}$
HCOO	−2.91	O$_{hcp}$	−3.03	O$_{hcp}$	−2.83	O$_{bri}$-C$_{top}$-O$_{top}$	−3.56	O$_{top}$-O$_{bri}$		
COOH	−2.00	C$_{bri}$-O$_{bri}$	−2.02	C$_{top}$-O$_{bri}$	−2.52	C$_{top}$-O$_{bri}$	−2.65	C$_{top}$-O$_{bri}$		
CH	−6.68	C$_{hcp}$	−6.70	C$_{hcp}$	−6.81	C$_{hcp}$	−6.97	C$_{hcp}$	−7.17	C$_{hcp}$
CH$_2$	−4.57	C$_{hcp}$	−4.60	C$_{hcp}$	−4.79	C$_{hcp}$	−4.90	C$_{hcp}$	−5.04	C$_{hcp}$
CH$_3$	−1.49	C$_{hcp}$	−1.66	C$_{hcp}$	−1.87	C$_{hcp}$	−2.36	C$_{hcp}$	−2.62	C$_{hcp}$
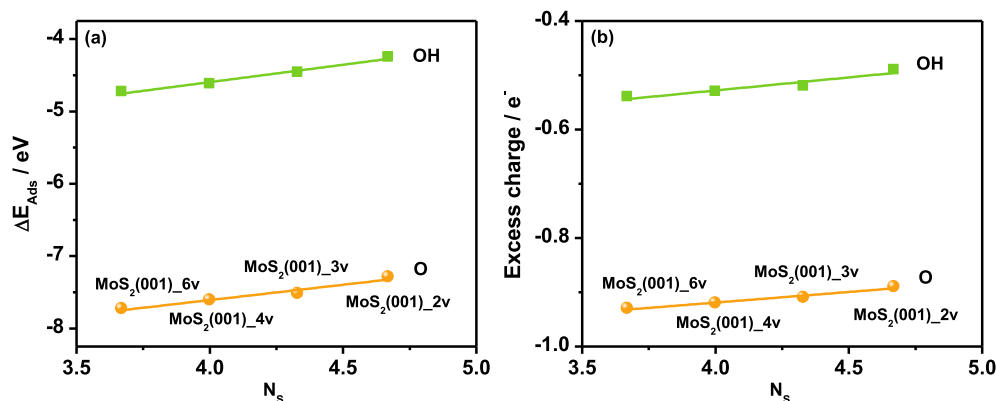
Fig. 9. (a) The adsorption energies ΔE_{Ads} of O (circle) and OH (square) and (b) the excess Bader charge of O (circle) and OH (square) plot against the number of S atoms coordinated to Mo atoms (N_S) at the favorable S vacancies of the $MoS_2(001)$ surfaces.

$5 \times 1/3 + 5 \times 1/3 + 4 \times 1/3 = 14/3$. Fig. 9a shows the ΔE_{Ads} of O and OH as a function of N_S on the $MoS_2(001)$ surfaces studied. It is found that the adsorption of O and OH is progressively weakened with increasing N_S from $MoS_2(001)\_6v$ to $MoS_2(001)\_2v$. This can be well explained because Mo atoms transfer more electrons to S atoms at higher N_S, leading to fewer electrons donation to the adsorbates and weaker binding at the S vacancies, as shown in Fig. 9b.

The linear relation between ΔE_{Ads} and N_S in Fig. 9a indicates that an increase in N_S can weaken O adsorption at the S vacancies on the $MoS_2(001)$ surfaces. However, finding a S vacancy configuration with higher N_S than on $MoS_2(001)\_2v$ is difficult. Only the $MoS_2(001)$ surface with a single S vacancy can fulfill the requirement, but this configuration can not catalyze C-O scission reactions that typically demand two S vacancies for the adsorption of dissociated fragments. These results suggest that irrespective of the morphologies and arrangement of sulfur vacancies the MoS_2 basal plane will not have high activity for the formation of CO, CH_4 and CH_3OH from CO_2 hydrogenation.

The commonly used catalysts for RWGS are the reducible oxide supported noble metal nanoparticles such as Ru, Ir and Pd, which always result in the byproducts of methane [24–28]. Although the selectivity of CO can be improved by reducing the size of metal nanoparticles, the resulting single-atom catalysts have been found to agglomerate into large nanoparticles under reaction conditions (350C^o, 1 bar and H_2/CO_2 = 3), leading to dramatic increase in methane selectivity [24]. Furthermore, these catalysts are still based on noble metals, which are more scarce and expensive than the MoS_2 catalyst. Thus, the MoS_2 catalyst can be a potential candidate for RWGS in terms of catalytic performance and price. The monodisperse SiO_2 nanospheres template, which can convert the Mo precursors (such as $(NH_4)_6Mo_7O_{24}$) into small MoS_2 domains, has be used to prepare the uniform mesoporous MoS_2 foam with plenty of edge sites [43]. By tuning the morphology of MoS_2 catalyst to expose more Mo edge sites, the activity of RWGS can be expected to be further improved.

4. Conclusions

Density functional theory calculations and microkinetic modeling have been used to identify the optimal type and morphology of S vacancy on MoS_2 catalyst for CO_2 hydrogenation and the key factors that control its performance. It is found that regardless of the morphologies of threefold sulfur vacancies on MoS_2 basal plane the relatively strong O binding causes O poisoning and low CO_2 hydrogenation activity at 580–780 K, 1 bar and H_2/CO_2 ratio of 1. The bridge S vacancy of the Mo edge, however, tunes the relative adsorption strength of key intermediates (such as O relative to OH) owing to its lower coordination number. This not only increases CO_2 hydrogenation rate by 7–11 orders of magnitude, but leads to noticeably different mechanism (associative

& redox). The large destabilization of O and low H coverage on the Mo edge also hinder C-O scission and hydrogenation (give CH_4 and CH_3OH) relative to CO desorption, leading to almost 100% CO selectivity. The work provides a mechanistic understanding into CO_2 hydrogenation on the inexpensive MoS_2 catalyst, and the coordination number of vacancies modulated catalytic performance can be applied to design and develop transition metal compound catalysts for other important reactions of technological interest.

CRediT authorship contribution statement

Hai-Yan Su: Conceptualization, Methodology, Writing - original draft. **Keju Sun:** Conceptualization, Software, Writing - review & editing. **Jin-Xun Liu:** Methodology, Writing - review & editing. **Xiufang Ma:** Formal analysis. **Minzhen Jian:** Formal analysis, Writing - review & editing. **Chenghua Sun:** Conceptualization, Software. **Yongjun Xu:** Formal analysis, Writing - review & editing. **Huibin Yin:** Writing - review & editing. **Wei-Xue Li:** Conceptualization, Methodology, Writing - review & editing.

Declaration of Competing Interest

The authors declare that they have no known competing financial interests or personal relationships that could have appeared to influence the work reported in this paper.

Appendix A. Supplementary material

Supplementary data to this article can be found online at https://doi.org/10.1016/j.apsusc.2021.149925.

References

[1] G. Pacchioni, Oxygen vacancy: the invisible agent on oxide surfaces, ChemPhysChem 4 (2003) 1041–1047.
[2] H.Y. Su, X.F. Ma, K.J. Sun, C.H. Sun, Y.J. Xu, F. Calle-Vallejo, Trends in C-O and N-O bond scission on rutile oxides described by oxygen vacancy formation energies, Chem. Sci. 11 (2020) 4119–4124.

[3] R. Schaub, P. Thostrup, N. Lopez, E. Lægsgaard, I. Stensgaard, J.K. Nørskov, F. Besenbacher, Oxygen vacancies as active sites for water dissociation on rutile TiO₂(110), Phys. Rev. Lett. 87 (2001), 266104.

[4] X. Wu, A. Selloni, S.K. Nayak, First principles study of CO oxidation on TiO₂(110): the role of surface oxygen vacancies, J. Chem. Phys. 120 (2004) 4512–4516.

[5] J.A. Rodriguez, S. Ma, P. Liu, J. Hrbek, J. Evans, M. Pérez, Activity of CeOₓ and TiOₓ nanoparticles grown on Au(111) in the water-gas shift reaction, Science 318 (2007) 1757–1760.

[6] F. Cheng, T. Zhang, Y. Zhang, J. Du, X. Han, J. Chen, Enhancing electrocatalytic oxygen reduction on MnO₂ with vacancies, Angew. Chem. Int. Ed. 52 (2013) 2474–2477.

[7] A. Grimaud, O. Diaz-Morales, B. Han, W.T. Hong, Y.-L. Lee, L. Giordano, K. A. Stoerzinger, M.T.M. Koper, Y. Shao-Horn, Activating lattice oxygen redox reactions in metal oxides to catalyse oxygen evolution, Nat. Chem. 9 (2017) 457–465.

[8] H. Y. Su, K. J. Sun, DFT study of the stability of oxygen vacancy in cubic ABO3 perovskites, J. Mater. Sci. 50 (2015) 1701–1709.

[9] M. Retuerto, F. Calle-Vallejo, L. Pascual, P. Ferrer, A. Garcia, J. Torrero, D. Gianolio, J.L.G. Fierro, M.A. Pena, J. Antonio Alonso, S. Rojas, Role of lattice oxygen content and Ni geometry in the oxygen evolution activity of the Ba-Ni-O system, J. Power Sources 404 (2018) 56–63.

[10] P.G. Moses, B. Hinnemann, H. Topsøe, J.K. Nørskov, The hydrogenation and direct desulfurization reaction pathway in thiophene hydrodesulfurization over Mo₂ catalysts at realistic conditions: a density functional study, J. Catal. 248 (2007) 188–203.

[11] S. Zaman, K.J. Smith, A review of molybdenum catalysts for synthesis gas conversion to alcohols: catalysts, mechanisms and kinetics, Catal. Rev. 54 (2012) 41–132.

[12] Q. Ma, P. M. Odenthal, J. Mann, D. Le, C. S. Wang, Y. Zhu, T. Chen, D. Sun, K. Yamaguchi, T. Tran, M. Wurch, J. L. McKinley, J. Wyrick, K. Magnone, T. F. Heinz, T. S. Rahman, R. Kawakami, L. Bartels, Controlled argon beam-induced desulfurization of monolayer molybdenum disulfide, J. Phys.: Condens. Matter 25 (2013) 252201.

[13] M.X. Liu, J.P. Shi, Y.C. Li, X.B. Zhou, D.L. Ma, Y. Qi, Y.F. Zhang, Z.F. Liu, Temperature-triggered sulfur vacancy evolution in monolayer MoS₂/graphene heterostructures, Small 13 (2017) 1602967.

[14] J. T. Hu, L. Yu, J. Deng, Y. Wang, K. Cheng, C. Ma, Q. H. Zhang, W. Wen, S. S. Yu, Y. Pan, J. Z. Yang, H. Ma, F. Qi, Y. K. Wang, Y. P. Zheng, M. S. Chen, R. Huang, S. H. Zhang, Z. C. Zhao, J. Mao, X. Y. Meng, Q. Q. Ji, G. J. Hou, X. W. Han, X. H. Bao, Y. Wang, D. H. Deng, Sulfur vacancy-rich MoS2 as a catalyst for the hydrogenation of CO2 to methanol, Nat. Catal. 2021, DOI: 10.1038/s41929-021-00584-3.

[15] H.-P. Komsa, J. Kotakoski, S. Kurasch, O. Lehtinen, U. Kaiser, A. V. Krasheninnikov, Two-dimensional transition metal dichalcogenides under electron irradiation: defect production and doping, Phys. Rev. Lett. 109 (2012) 035503.

[16] T. Osaki, N. Narita, T. Horiuchi, T. Sugiyama, H. Masuda, K. Suzuki, Kinetics of reverse water gas shift (RWGS) reaction on metal disulfide catalysts, J. Mol. Catal. A: Chem. 125 (1997) 63–71.

[17] L. Sharma, R. Upadhyay, S. Rangarajan, J. Baltrusaitis, Inhibitor, Co-catalyst, or Co-reactant? probing the different roles of H₂S during CO₂ hydrogenation on MoS₂ catalyst, ACS Catal. 9 (2019) 10044–10059.

[18] A. Primo, J.B. He, B. Jurca, B. Cojocaru, C. Bucur, V.I. Parvulescu, H. Garcia, CO₂ methanation catalyzed by oriented MoS₂ nanoplatelets supported on few layers graphene, Appl. Catal. B: Environmental 245 (2019) 351–359.

[19] Q. Liu, L.P. Wu, R. Jackstell, M. Beller, Using carbon dioxide as a building block in organic synthesis, Nat. Commun. 6 (2015) 5933.

[20] N. von der Assen, P. Voll, M. Peters, A. Bardow, Life cycle assessment of CO2 capture and utilization: a tutorial review, Chem. Soc. Rev. 43 (2014) 7982–7994.

[21] M. Aresta, A. Dibenedetto, A. Angelini, Catalysis for the valorization of exhaust carbon: from CO₂ to chemicals, materials, and fuels. technological use of CO₂, Chem. Rev. 114 (2014) 1709–1742.

[22] E.L. Kunkes, F. Studt, F. Abild-Pedersen, R. Schlogl, M. Behrens, Hydrogenation of CO₂ to methanol and CO on Cu/ZnO/Al₂O₃: Is there a common intermediate or not? J. Catal. 328 (2015) 43–48.

[23] J. Klankermayer, S. Wesselbaum, K. Beydoun, W. Leitner, Selective catalytic synthesis using the combination of carbon dioxide and hydrogen: Catalytic chess at the interface of energy and chemistry, Angew. Chem. Int. Ed. 55 (2016) 7296–7343.

[24] J.H. Kwak, L. Kovarik, J. Szanyi, CO₂ reduction on supported Ru/Al₂O₃ catalysts: cluster size dependence of product selectivity, ACS Catal. 3 (2013) 2449–2455.

[25] J.H. Kwak, L. Kovarik, J. Szanyi, Heterogeneous catalysis on atomically dispersed supported metals: CO₂ reduction on multifunctional Pd catalysts, ACS Catal. 3 (2013) 2094–2100.

[26] J.C. Matsubu, V.N. Yang, P. Christopher, Isolated metal active site concentration and stability control catalytic C₀2 reduction selectivity, J. Am. Chem. Soc. 137 (2015) 3076–3084.

[27] X.D. Chen, X. Su, H.Y. Su, X.Y. Liu, S. Miao, Y.H. Zhao, K.J. Sun, Y.Q. Huang, T. Zhang, Theoretical insights and the corresponding construction of supported metal catalysts for highly selective C₀2 to CO conversion, ACS Catal. 7 (2017) 4613–4620.

[28] S.W. Li, Y. Xu, Y.F. Chen, W.Z. Li, L.L. Lin, M.Z. Li, Y.C. Deng, X.P. Wang, B.H. Ge, C. Yang, S.Y. Yao, J.L. Xie, Y.W. Li, X. Liu, D. Ma, Tuning the selectivity of catalytic carbon dioxide hydrogenation over iridium/cerium oxide catalysts with a strong metal–support interaction, Angew. Chem. Int. Ed. 56 (2017) 10761–10765.

[29] G. Kresse, J. Furthmüller, Efficient iterative schemes for ab initio total-energy calculations using a plane-wave basis set, Phys. Rev. B 54 (1996) 11169–11186.

[30] J.P. Perdew, K. Burke, M. Ernzerhof, Generalized gradient approximation made simple, Phys. Rev. Lett. 77 (1996) 3865–3868.

[31] P. E. Blöchl, Projector augmented-wave method, Phys. Rev. B 50 (1994) 17953–17979.

[32] F. Jellinek, G. Brauer, H. Müller, Molybdenum and niobium sulphides, Nature 185 (1960) 376–377.

[33] H.J. Monkhorst, J.D. Pack, Special points for brillouin-zone integrations, Phys. Rev. B 13 (1976) 5188–5192.

[34] G. Henkelman, H. Jonsson, Improved tangent estimate in the nudged elastic band method for finding minimum energy paths and saddle points, J. Chem. Phys. 113 (2000) 9978.

[35] K.J. Sun, Y.H. Zhao, H.Y. Su, W.X. Li, Force reversed method for locating transition states, Theo. Chem. Acc. 131 (2012) 1118.

[36] I. A. W. Filot, R. A. van Santen, E. J. M. Hensen, The optimally performing Fischer–Tropsch catalyst, Angew. Chem. Int. Ed. 53 (2014) 12746–12750.

[37] X.R. Shi, H.J. Jiao, K. Hermann, J.G. Wang, CO hydrogenation reaction on sulfided molybdenum catalysts, J. Mol. Catal. A: Chem. 312 (2009) 7–17.

[38] H.Y. Su, X.F. Ma, C.H. Sun, K.J. Sun, Synergetic effect between single Cu site and S vacancy on MoS₂ basal plane for methanol synthesis from syngas, Catal. Sci. Technol. (2021), https://doi.org/10.1039/D1CY00003A.

[39] M. J. L. Ginés, A. J. Marchi, C. R. Apesteguía, Kinetic study of the reverse water-gas shift reaction over CuO/ZnO/Al2O3 catalysts, Appl. Catal. Gen. 154 (1997) 155–171.

[40] T. Shido, Y. Iwasawa, The effect of coadsorbates in reverse water-gas shift reaction on ZnO, in relation to reactant-promoted reaction mechanism, J. Catal. 140 (1993) 575–584.

[41] C. Stegelmann, A. Andreasen, C.T. Campbell, Degree of rate control: how much the energies of intermediates and transition states control rates, J. Am. Chem. Soc. 131 (2009) 8077–8082.

[42] H.Y. Su, Y. Gorlin, I.C. Man, F. Calle-Vallejo, J.K. Norskov, T.F. Jaramillo, J. Rossmeisl, Identifying active surface phases for metal oxide electrocatalysts: a study of manganese oxide bi-functional catalysts for oxygen reduction and water oxidation catalysis, Phys. Chem. Chem. Phys. 14 (2012) 14010–14022.

[43] J. Deng, H.B. Li, S.H. Wang, D. Ding, M.S. Chen, C. Liu, Z.Q. Tian, K.S. Novoselov, C. Ma, D.H. Deng, X.H. Bao, Multiscale structural and electronic control of molybdenum disulfide foam for highly efficient hydrogen production, Nat. Commun. 8 (2017) 14430.